



MOF-derived N-doped carbon nanosticks coupled with Fe phthalocyanines for efficient oxygen reduction

Yuandong Yang^{a,b}, QiuHong Sun^a, Jinhang Xue^a, Shaojie Xu^a, Lujiao Mao^a, Tingting Miao^a, Linjie Zhang^b, Jinjie Qian^{a,*}

^a College of Life and Environmental Science & College of Chemistry and Materials Engineering, Wenzhou University, Wenzhou, Zhejiang 325035, PR China

^b State Key Laboratory of Structure Chemistry, Fujian Institute of Research on the Structure of Matter, Chinese Academy of Sciences, Fuzhou, Fujian 350002, PR China

ARTICLE INFO

Keywords:

Metal-organic framework
Carbon nanomaterial
Iron phthalocyanine
Molecular catalyst
Oxygen reduction reaction

ABSTRACT

The rational design and preparation of atomic-level dispersed non-platinum catalysts to achieve efficient oxygen reduction reactions (ORR) is worth exploring for clean energy conversion and storage technology. Herein a simple self-templating strategy is demonstrated to obtain MIL-68-NH₂-x series using pyridine as a surfactant to realize micron-scale to nanosized conversion. Among them, the as-prepared MIL-68-NH₂-300 owns a large specific surface area and abundant pore defects after thermal treatment, which can effectively adsorb and anchor Fe phthalocyanines (FePc). In this case, MOF-derived N-doped carbon nanosticks coupled with FePc molecules (FePc@NCNS) exhibit an excellent electrocatalytic ORR activity with a positive half-wave potential (0.904 V), a large diffusion-limited current density (6.17 mA cm⁻²) and a high current retention after 20 h (95.7%). Furthermore, the high performance of ORR is confirmed by the relevant theoretical calculations on O₂ adsorption ability. These above results will pave the way for MOF-derived carbon nanomaterials with specific morphological dimensions for high-performance energy conversion and storage.

1. Introduction

In recent years, the Chinese government has released a dual carbon strategy to reach peak carbon emissions before 2030, and achieve carbon neutrality before 2060. It implies the gradual withdrawal of traditional fossil fuels and their replacement by new green energy sources that are aimed at promoting environmental protection and implementing a low-carbon and sustainable path to quality development [1–3]. Among them, rechargeable hydrogen–oxygen fuel cells and metal-air batteries with green, high efficiency and high energy density have attracted numerous attention [4,5]. However, while offering many advantages, the above devices are severely hampered in practical applications on account of the slow kinetics of oxygen reduction reaction (ORR) at the cathode [6,7]. To solve this problem, platinum-based catalysts have been extensively studied owing to their high catalytic activity and selectivity for ORR. However, their high cost, low reserve, poor stability and easy poisoning in the electrolytes limit their large-scale applications [8,9]. On the other hand, transition metal-nitrogen-carbon (M–N–C) nanomaterials to mimic the core of heme have been demonstrated as efficient alternatives to precious metal catalysts

[10,11]. Under these circumstances, the rational design and convenient preparation of cost-effective, high-activity and robust-stability M–N–C based ORR catalysts are of great importance.

Metal-organic frameworks (MOFs), an emerging subclass of organic–inorganic hybrids, have been widely used in the preparation of M–N–C nanomaterials due to their tunable morphology, adjustable nanostructure, rich topology, and abundant porous properties [12–14]. MOF-derived M–N–Cs have received much attention as a result of their larger specific surface area, higher space utilization, and more exposed active species than bulk materials [15,16]. Although researchers are skilled to utilize the template method to control MOF-derived carbon nanomaterials with more pores, the actual preparation process is usually complex and time-consuming [17,18]. In order to achieve more active sites, it is worth exploring the simplified surface modification to realize the desired morphology and the reduced size of MOF-derived nanomaterials for effective heterogeneous catalysis.

On the other hand, a series of MOF-derived M–N–C nanomaterials have been reported as highly active ORR catalysts. However, during the thermal treatment, the inorganic metals in MOF precursors are highly prone to aggregate and form clusters, which in turn weakens the

* Corresponding author.

E-mail address: jinjieqian@wzu.edu.cn (J. Qian).

<https://doi.org/10.1016/j.cej.2023.142668>

Received 7 February 2023; Received in revised form 17 March 2023; Accepted 26 March 2023

Available online 29 March 2023

1385-8947/© 2023 Elsevier B.V. All rights reserved.

performed electrocatalytic activity [19,20]. Therefore, single-atom catalysts become popular for their maximized atom utilization, but it is hard to modulate the metal atom dispersion when preparing atomically dispersed catalysts [21,22]. In this context, metal phthalocyanine (MPc), as one typical M–N₄ macrocycle, stands out for the facile syntheses of molecular catalysts with excellent ORR activity [23,24]. However, the requirements for the selection of carbon carriers such as carbon nanotubes, graphene, etc. for such molecular catalysts are extremely stringent [25,26]. The stability of most of the carbon carrier catalysts is not sufficient under repeated start-stop cycling and high potential conditions of the corresponding devices. Among others, oxidative corrosion of the carbon support has been identified as a major cause of electrocatalyst performance degradation and lifetime shortening, which can lead to aggregation, dissolution and detachment of the loaded metal active centers [27–29]. Therefore, the easy fabrication of suitable MOF-derived carbon substrates for anchoring MPc molecules to achieve efficient and stable ORR remains challenging to a large extent.

In this work, a stepwise synthetic strategy to obtain MOF-derived porous carbons with FePc molecules by modulating the morphology is reported as depicted in Scheme 1. First of all, one type of stick-shaped indium-based MIL-68-NH₂ has been successfully synthesized whose sizes could be effectively regulated by adding pyridine. The obtained MIL-68-NH₂-x series (x indicates different concentrations of pyridine, 0–300 μL) gradually become slimmer with the increase of pyridine content. Afterwards, they are thermally converted into porous carbon substrates with abundant structural defects and high graphitization, which will be more favorable for space confinement of FePc. Finally, these MOF-derived N-doped carbon nanosticks loaded with FePc molecules (FePc@NCNS) exhibit satisfactory ORR performance, where the half-wave voltage is 0.904 V, the onset voltage is 0.978 V, and the limited current density is 6.17 mA cm⁻², which are competitive to the state-of-the-art catalyst of Pt/C.

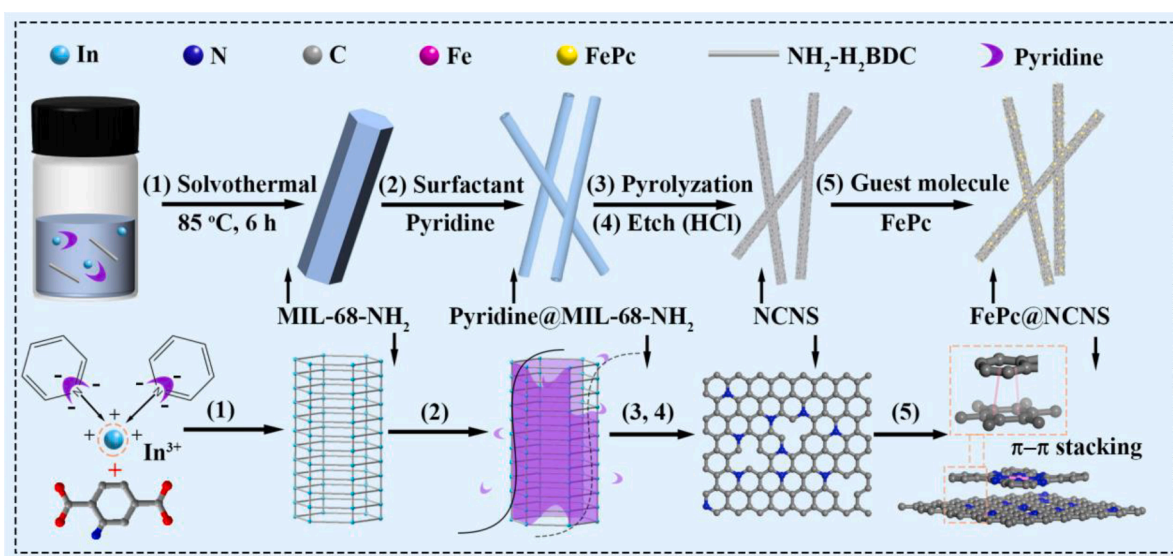
2. Results and discussions

The stick-shaped MIL-68-NH₂ can be conveniently obtained by self-assembly between indium salt and 2-aminoterephthalic acid (NH₂-H₂BDC), more detailed synthetic procedure please see the experimental part in Supporting Information. In its asymmetric unit, there are one-third deprotonated and half a deprotonated NH₂-BDC²⁻, together with half a 6-coordinated In(III) cation (Fig. 1a, S1, Table S1). It is worth noting that six NH₂-BDC²⁻ linkers are connected to six In(III) centers on the (001) plane to form a regular hexagonal channel of ~ 18.2 Å

(Fig. S2). From optical microscope and SEM images in Fig. 1b, S3, these crystals present hexagonal columnar morphology with an average diameter of 300 nm. Furthermore, the PXRD analysis reveals two sharp diffraction peaks at 8.1° and 9.3° corresponding to (200) and (220) planes, respectively, well consistent with the simulated pattern to confirm the high purity and crystallinity of as-synthesized coordination polymers (Fig. 1c). In Fig. 1d, the TGA curve shows a continuous transition where Steps I-II belong to the removal of guest molecules and the gradual collapse of overall coordination network, and Step III is ascribed to the carbonization of organic linkers. Meanwhile, the collected N₂ curves of desolvated sample exhibit Type-IV sorption isotherms, and the pore size distribution (PSD) verifies the microporous nature mainly at 0.54 nm (Fig. 1e, f).

To synthesize nanoscale MOFs with a larger specific surface area and smaller particle size, pyridine is further added for surface modification. Due to the high electron negativity of the N atom, pyridine will be adsorbed around the positive In(III) center as well as the external crystal surface during subsequent crystal growth (Fig. S4) [30,31]. Interestingly, when different amounts of pyridine are inserted, the obtained MIL-68-NH₂-x series (x = 0–300 μL) are gradually transformed from large hexagonal prisms of 15 μm to thin sticks of 300 nm (Fig. 2a–f, S5). In Fig. 2g, h, two discernable diffraction peaks for the (200) and (220) planes are clearly observed to prove that the obtained MOFs retain high crystallinity after adding pyridine. In the meantime, the (200) crystal plane at 8.1° gradually widens to imply that it is more preferentially attached onto the (200) facet which inhibits the lateral accumulation of crystals [32]. PXRD patterns are well matched with the structural and morphological change, which reveals MIL-68-NH₂ crystals to grow anisotropically. In Fig. 2i, the Type-IV N₂ isotherms and their PSD profiles show a narrow distribution near the 0.5 nm region. Among them, MIL-68-NH₂-300 gives a maximum specific surface area of 300.62 m² g⁻¹ and a total pore volume of 0.2402 cm³ g⁻¹ (Table S2). On this basis, an increase in porosity can be interpreted as the nano-effect of MOF crystals, which would provide a favorable condition for the encapsulation of guest molecules as well as the formation of porous MOF-derived carbon nanomaterials.

By pyrolysis of MIL-68-NH₂-300, one type of hierarchically porous N-doped carbon nanosticks (NCNS) can be conveniently obtained (Fig. S6). It would facilitate the introduction of discrete FePc molecules into large pores of MOF-derived porous carbons to give the final product of FePc@NCNS in Fig. 3a, S7. Besides, the molten indium species will effectively evaporate during calcination, thus generating more micro-/meso-pores conducive to the adsorption of FePc to form a stable



Scheme 1. Stepwise fabrication of pyridine-modified MIL-68-NH₂ derived porous carbon nanomaterial of FePc@NCNS.

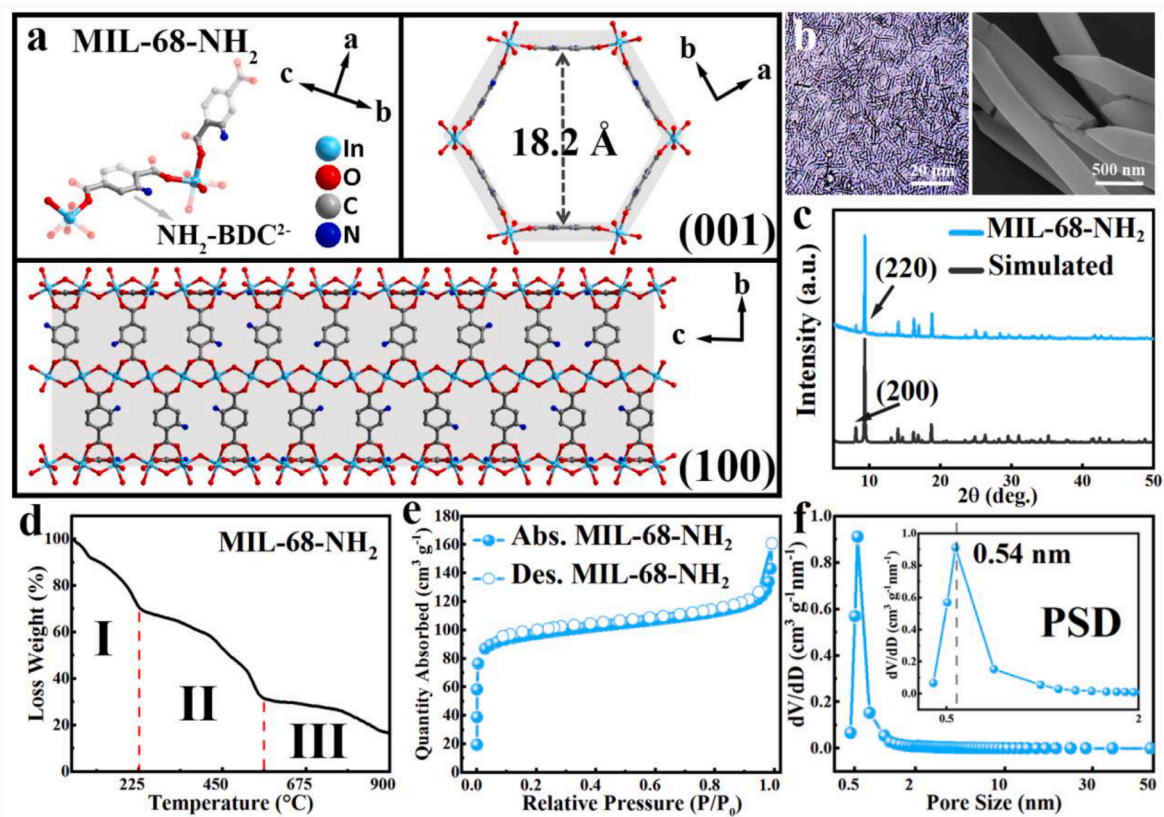


Fig. 1. MIL-68-NH₂: (a) The asymmetric unit and structural features; (b) Optical and SEM images; (c) PXRD patterns; (d) TGA curve; (e) N₂ isotherms; (f) PSD analysis, the inset corresponds to its microporous region.

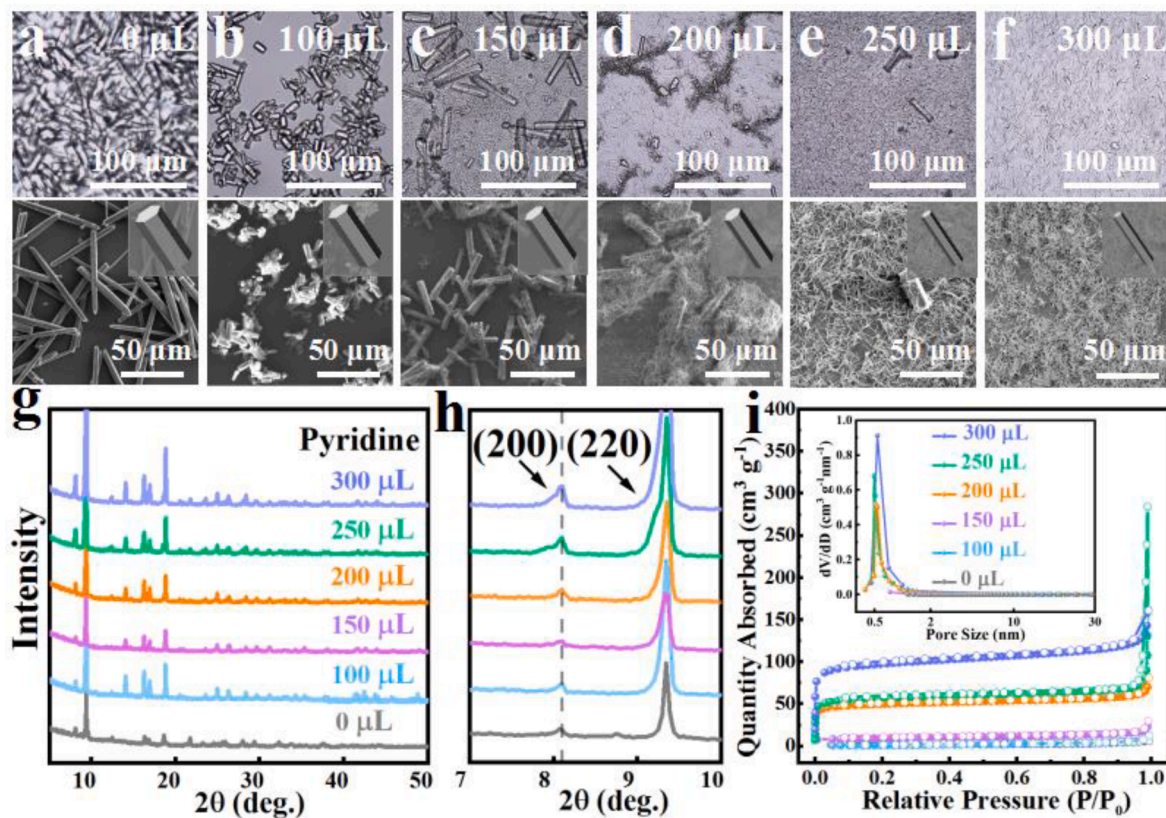


Fig. 2. MIL-68-NH₂-x (x = 0–300 μL) series: (a–f) Optical and SEM images; (g–h) PXRD patterns and its enlarged region in 7–10°; (i) N₂ isotherms and PSD analysis.

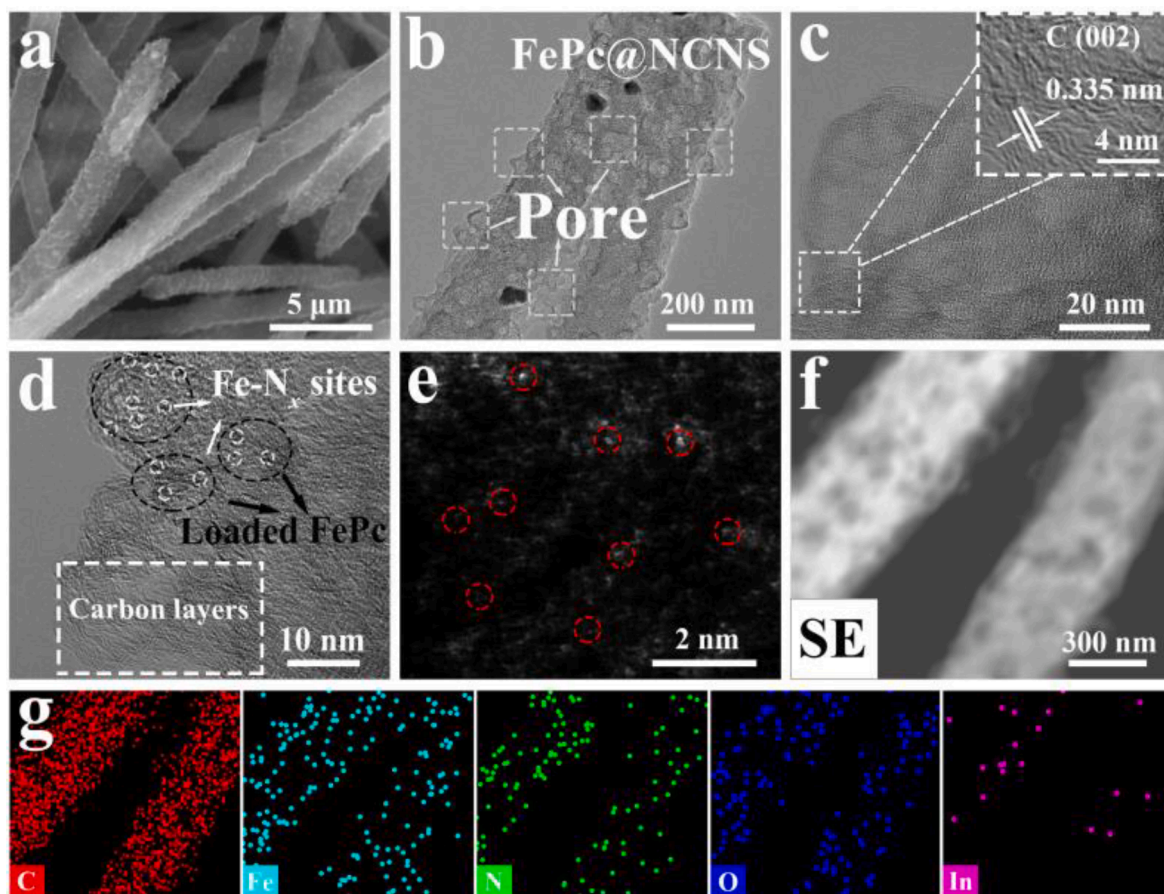


Fig. 3. (a-e) SEM, TEM, HR-TEM and AC-HAADF-STEM images of FePc@NCNS; (f-g) HAADF-STEM images and EDS mappings of FePc@NCNS.

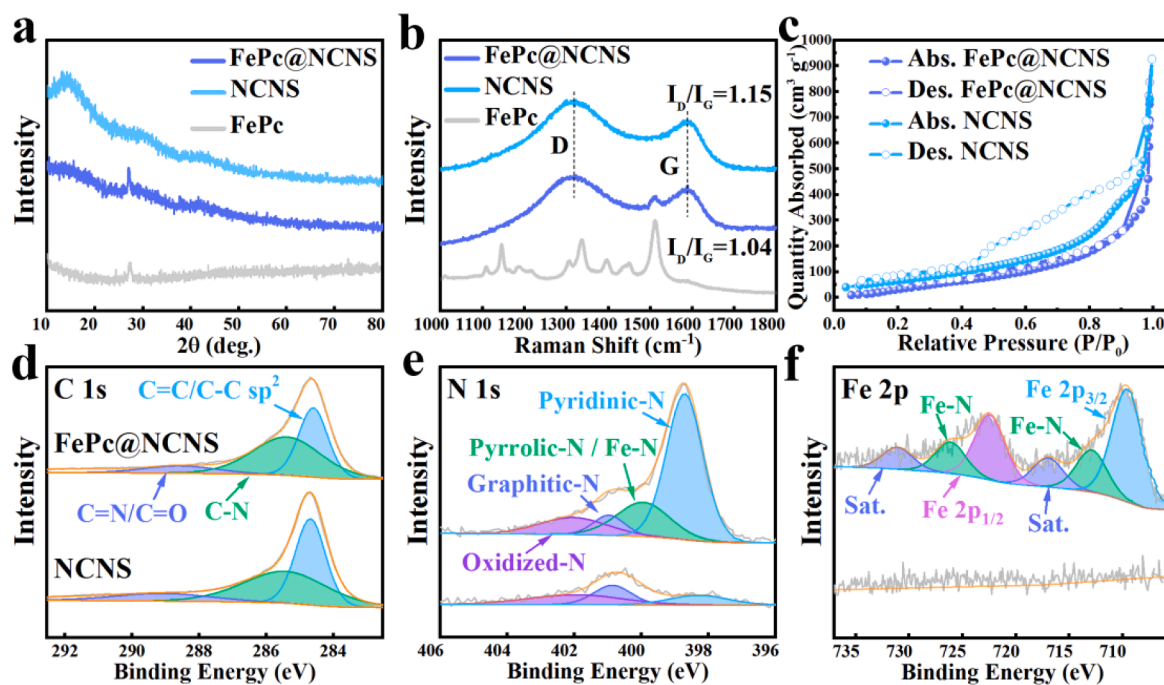


Fig. 4. (a) PXRD patterns of FePc@NCNS, NCNS and FePc; (b) Raman spectra of FePc@NCNS, NCNS and FePc; (c) N₂ isotherms of FePc@NCNS and NCNS; The deconvoluted XPS spectra of FePc@NCNS and NCNS: (d) C 1s, (e) N 1s, (f) Fe 2p.

nanocomposite. In Fig. 3b, its TEM image reveals a large number of structural defects formed by high temperature calcination. Although it is accompanied by the collapse of MOF structure, the original stick morphology is still roughly retained due to the high stability of the precursor. High-resolution TEM (HR-TEM) images present the lattice fringes of 0.335 nm, ascribing to the (002) plane of the graphitic carbon (Fig. 3c). As shown in Fig. 3d, S8, the obtained FePc@NCNS shows a distinct dark spot on the carbon layers to reflect the successful loading of FePc. In this case, the carbon layer and FePc guest are effectively coupled through π - π stacking, while the strong chemical and electronic coupling between electron-rich defects and electron-deficient Fe atoms avoids a large aggregation of FePc to expose more active Fe sites [33,34]. Based on this, it will largely increase the possibility of adsorption of Fe-N₄ active centers with O₂ and thus significantly improve the ORR performance of the material. To elucidate the state of the Fe atoms, aberration-corrected high-angle annular dark field scanning TEM (AC-HAADF-STEM) measurement is further carried out in Fig. 3e. On account of the structural characteristics of FePc molecules, the Fe atoms in FePc@NCNS are most probably in a similar form to pure FePc and well distributed at the atomic level [25,35]. Furthermore, the HAADF-STEM image, element mapping, and energy dispersive X-ray spectrum (EDS) certify the uniform distribution of C, N, O, In and Fe (Fig. 3f, g).

In Fig. 4a, FePc@NCNS owns an obvious peak at 27.1° similar to pure FePc, which further proves the successful loading of FePc. In addition, the calculated I_D/I_G ratio of FePc@NCNS (1.04) is smaller than NCNS of 1.15 (Fig. 4b), implying that the loaded FePc is beneficial to the

improved degree of graphitization. Their Type-III isotherms show the calculated specific surface areas of 274.9 and 286.6 m² g⁻¹ for FePc@NCNS and NCNS, respectively (Fig. 4c, Table S2). In this case, the reduced surface area is mainly ascribed to the partially blocked pores by FePc, while PSD curves confirm the retained micropores of ~ 2 nm in Fig. S9. The XPS spectra show the obvious peaks of C 1s, O 1s, and N 1s, Fe 2p and subtle signals of In 3d for all samples (Fig. S10). The high-resolution C 1s spectra can be deconvoluted into three separate peaks of C=C/C-C (284.6 eV), C-N (285.5 eV), and C=N/C=O (288.7 eV) in Fig. 4d. And the N 1s spectra can be divided into pyridinic-N (398.6 eV), pyrrolic-N/Fe-N (399.8 eV), graphitic-N (400.9 eV), and oxidized-N (402.2 eV), respectively (Fig. 4e). Previously, some studies suggest that pyridinic-N provides suitable Lewis base sites to strongly chemisorb O₂ molecules for efficient ORR [25,36]. Furthermore, FePc@NCNS exhibits a stronger pyrrolic-N/Fe-N peak at 399.8 eV, which is attributed to the fact that FePc as the main active center provides abundant Fe-N₄ active sites. In Fig. 4f, the high-resolution Fe 2p curves are split into three pairs of peaks: the first two satellite peaks appear at 717.1/731.2 eV; the second belongs to the coordination environment of Fe-N at 713.1/726.3 eV; the last pair shows Fe 2p_{1/2} (722.6 eV) and Fe 2p_{3/2} (709.8 eV), respectively. Notably, the Fe 2p_{3/2} peak is located near 710.2 eV, indicating that the Fe valence state in FePc@NCNS is close to +3. Meanwhile, when Fe(III) in the active center is coordinated with pyrrole N atoms of the N-doped carbon carrier, the oxidation state of the +3 valence state can be maintained by electronic coupling during electrocatalysis, thus providing superior adsorption sites and active sites, which will greatly enhance the ORR activity of the material to a

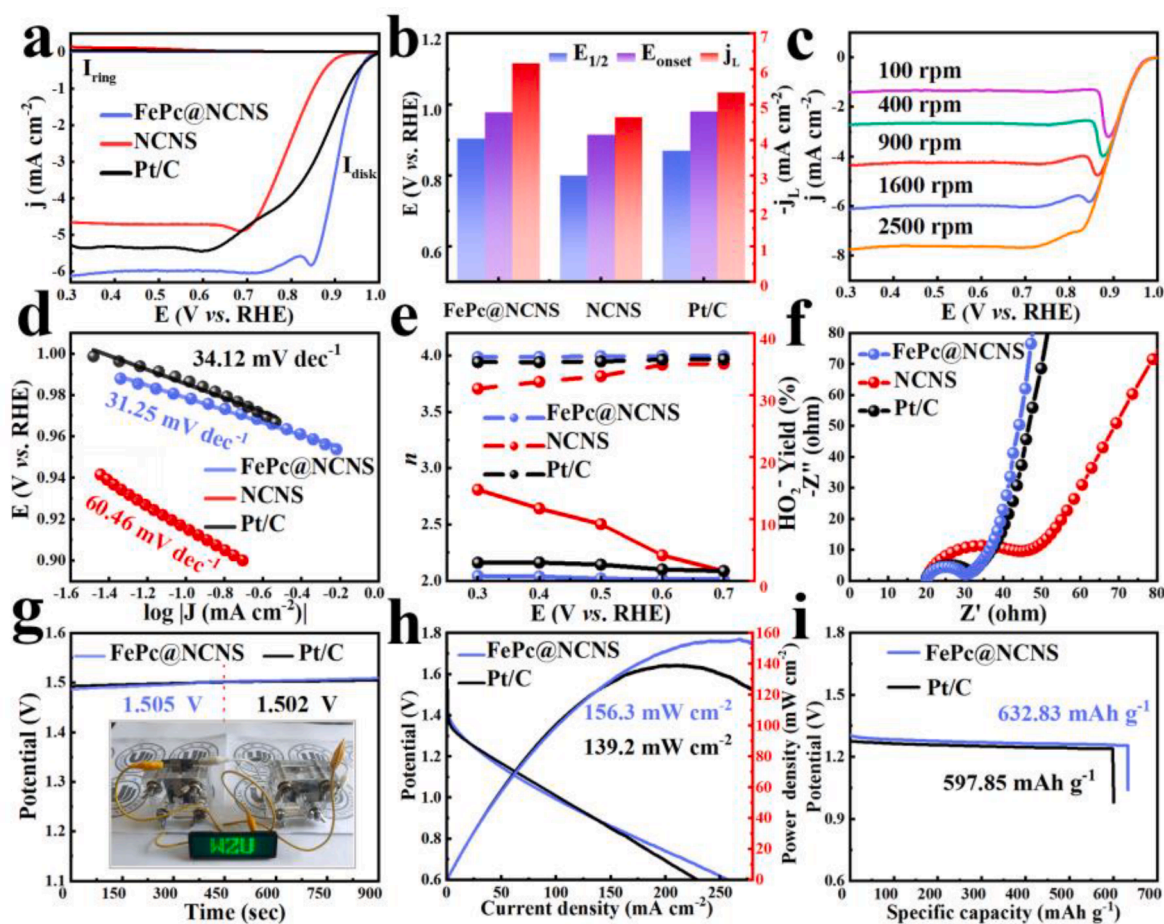


Fig. 5. (a) LSV curves at 1600 rpm of FePc@NCNS, NCNS and Pt/C; (b) Comparison of $E_{1/2}$, E_{onset} and J_1 of FePc@NCNS, NCNS and Pt/C; (c) LSV curves at various rotation rates of FePc@NCNS; (d) Tafel slopes of FePc@NCNS, NCNS and Pt/C; (e) n and HO_2^- yield of FePc@NCNS, NCNS and Pt/C; (f) EIS plots of FePc@NCNS, NCNS and Pt/C; (g) OCV profiles of FePc@NCNS and Pt/C; (h) Polarization and power density curves of FePc@NCNS and Pt/C; (i) Galvanostatic discharge curves of FePc@NCNS and Pt/C.

large extent [37,38]. For O 1s, two peaks of C–O and M–O can be distinguished, while two more peaks come from In 3d_{5/2} and 3d_{3/2}, indicating that a few indium species still exist in the carbon layer (Figs. S11, 12).

As a result of numerous Fe-N₄ sites, the obtained FePc@NCNS is expected to exhibit excellent electrochemical performance. First, CV measurements clearly show the ORR peak position of FePc@NCNS (0.925 V) close to Pt/C (0.938 V) and much higher than NCNS (0.731 V) in Fig. S13. LSV curves present the onset potential (E_{onset}) at -0.1 mA cm⁻², half-wave voltage ($E_{1/2}$) and diffusion-limited current density (J_L) at 0.3 V (Fig. 5a, b). In this case, FePc@NCNS is calculated to be 0.978 V, 0.904 V and 6.17 mA cm⁻², respectively, better than those of Pt/C (0.981 V, 0.870 V and 5.35 mA cm⁻²), NCNS (0.915 V, 0.801 V, 4.65 mA cm⁻²) and those reported catalysts (Table S3). The above results indicate that FePc@NCNS has a more positive onset potential than that of NCNS, suggesting that oxygen molecules can be conveniently reduced at the Fe-N₄ sites under a smaller overpotential. LSV curves at different rotation speeds and the corresponding K-L plots imply the diffusion-controlled ORR property in Fig. 5c, S14, 15. And the fitted Tafel slopes are 31.25, 34.12 and 60.46 mV dec⁻¹ for FePc@NCNS, Pt/C and NCNS, respectively, to reflect the former with the fastest reaction kinetics (Fig. 5d). In Fig. S16, the electrochemical C_{d1} value is 31.42 mF cm⁻² for FePc@NCNS, also higher than these control samples. Fig. 5e reveals the average electron transfer number (n) and H₂O₂ yield of

FePc@NCNS of 3.99 and 0.82% to verify a quasi-4-electron pathway. It owns the lowest charge transfer resistance (R_{ct}) of 10.648 Ω which would facilitate the electron transfer (Fig. 5f, S17, Table S4). On the other hand, the current retention of FePc@NCNS after 20 h (95.7%) is higher than Pt/C of 87.9% (Fig. S18) stemming from the strong intermolecular interaction between graphitic NCNS and FePc [16,27]. After MeOH is added, its current density remains almost unchanged, while Pt/C owns a poor methanol resistance (Fig. S19). As anticipated, its open-circuit voltage (OCV), peak power density, and specific capacity of the assembled ZAB is calculated to be 1.505 V, 156.3 mW cm⁻² and 632.83 mA h g⁻¹, respectively, competitive to Pt/C (1.502 V, 135.2 mW cm⁻² and 597.85 mA h g⁻¹) in Fig. 5g-i. The above results demonstrate that FePc@NCNS exhibits better performance in both catalytic activity, stability and practical application to make it a promising alternative to Pt/C.

The theoretical calculations are carried out to further understand the synergistic effects of FePc and NCNS on ORR activity. In this case, two geometrically optimized models are reasonably constructed to elucidate the adsorption behavior of O₂. It is worth noting that the core of FePc molecule is chosen as the main configuration modeling that acts as the active Fe-N₄ site (Fig. S20). In Fig. 6a and Table S5, the adsorption energy (E_a) of FePc@NCNS (-5.126 eV) is much lower than that of NCNS (-5.030 eV), which can be well explained by the stronger adsorption capacity of Fe-N₄ sites for O₂. In addition, the valence electron

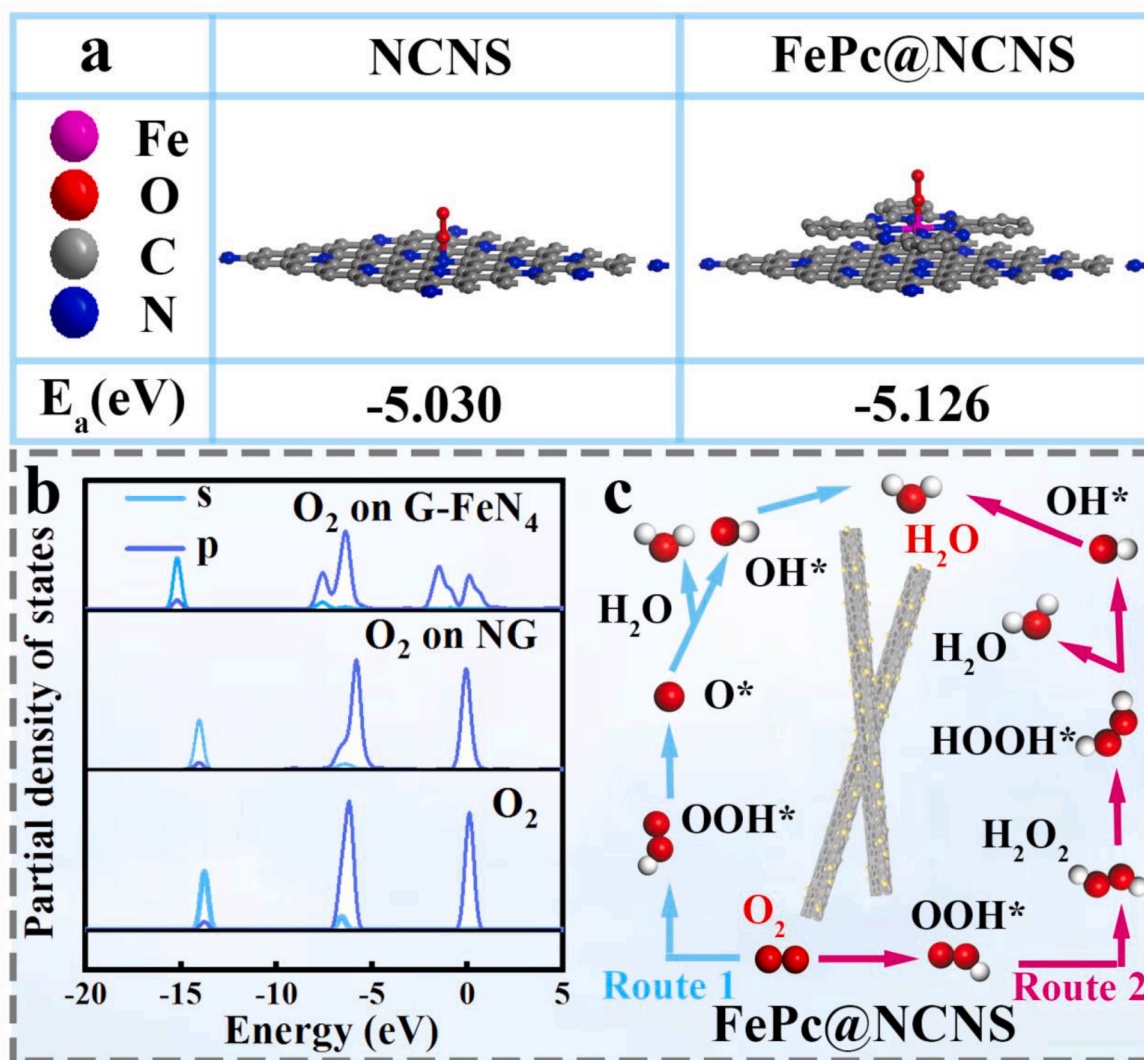


Fig. 6. (a) Theoretically optimized models of NCNS and FePc@NCNS; (b) PDOS after the adsorption of O₂ on NG and G-FeN₄; (c) Two plausible ORR pathways.

hybridization energy broadening is evident at 0 and -6.28 eV for the partial density of states (PDOS) of O_2 in NCNS and FePc@NCNS compared to free-standing O_2 molecule (Fig. 6b). This is mainly attributed to the strong interaction between O_2 molecules and Fe- N_4 active sites, which can be better explained by the tendency of the empty orbitals of Fe atoms on FePc@NCNS to accommodate the electrons transferred from oxygen, which is responsible for the potential oxygen adsorption and oxygen activation [30,39,40]. Moreover, Fig. 6c consists of two general ORR reaction mechanism: the typical 4-electron direct pathway (Route 1) and the combined pathway (Route 2). Among them, Fe- N_4 as the catalytically active center and its weak H_2O_2 yield (0.82%) proves that FePc@NCNS takes a typical 4-electron ORR mechanism [41,42]. In detail, $*O_2$ adsorbed on the carbon surface reacts with one proton and one electron to generate $*OOH$, which is then decomposed into $*O$ and $*OH$ radicals. After that, $*OH$ is reduced to give the first H_2O molecule, and the remaining $*O$ reacts with one proton and one electron to form $*OH$, which is further reduced to form the second H_2O .

3. Conclusion

In conclusion, one type of In-based MIL-68- NH_2 nanosticks has been successfully modulated by using pyridine, which is further pyrolyzed to form porous carbon nanomaterial. Furthermore, dispersed FePc molecules are effectively coupled into MOF-derived N-doped carbon nanosticks of NCNS. Owing to a large number of structural defects and high graphitization degree, this composite is intrinsically endowed with more exposed active sites, fast transfer for electrons as well as O_2 . Hence, the as-prepared FePc@NCNS exhibits excellent electrocatalytic ORR activity with a positive E_{onset} value of 0.978 V and a large J_1 value of 6.17 mA cm^{-2} , which are parallel to that of Pt/C. It also shows that the FePc@NCNS based ZAB holds satisfactory performance with large OCV value, peak power density as well as good stability to firmly demonstrate its practical applications. In the meantime, the theoretical results further reveal that the electron-rich nanostructure induced by defects in FePc@NCNS accelerates the adsorption and reduction of O_2 molecules on Fe atoms. All in all, the experimental and computational data confirm that FePc-loaded carbon nanomaterial preferentially adsorbs O_2 and reduces its reaction activation energy, which is mainly attributed to the introduction of Fe- N_4 active centers strongly promoting the ORR reaction.

Authors contribution

All authors contributed extensively to this work. J. Qian conceived the research project. Y. Yang conducted the experiments and performed the characterization studies. Y. Yang wrote the manuscript with input from all co-authors, and they have given approval to the final version of the manuscript.

Declaration of Competing Interest

The authors declare that they have no known competing financial interests or personal relationships that could have appeared to influence the work reported in this paper.

Data availability

Data will be made available on request.

Acknowledgements

This work was financially supported by National Natural Science Foundation of China (21601137), Natural Science Foundation of Zhejiang Province (LQ16B010003), Basic Science and Technology Research Project of Wenzhou, Zhejiang Province (H20220001, G20190007), and the Special Basic Cooperative Research Programs of Yunnan Provincial

Undergraduate Universities Association (202101BA070001-042).

Appendix A. Supplementary data

Supplementary data to this article can be found online at <https://doi.org/10.1016/j.cej.2023.142668>.

References

- [1] Z.W. Seh, J. Kibsgaard, C.F. Dickens, I. Chorkendorff, J.K. Nørskov, T.F. Jaramillo, Combining theory and experiment in electrocatalysis: insights into materials design, *Science* 355 (2017) 379380.
- [2] R. Paul, L. Zhu, H. Chen, J. Qu, L.M. Dai, Recent advances in carbon-based metal-free electrocatalysts, *Adv. Mater.* 31 (2019) 1806403.
- [3] L. Dai, Y. Xue, L. Qu, H.-J. Choi, J.-B. Baek, Metal-free catalysts for oxygen reduction reaction, *Chem. Rev.* 115 (11) (2015) 4823–4892.
- [4] M. Xiao, J. Zhu, G. Li, N.a. Li, S. Li, Z.P. Cano, L.u. Ma, P. Cui, P. Xu, G. Jiang, H. Jin, S. Wang, T. Wu, J. Lu, A. Yu, D. Su, Z. Chen, A single-atom iridium heterogeneous catalyst in oxygen reduction reaction, *Angew. Chem. Int. Ed.* 58 (28) (2019) 9640–9645.
- [5] X.X. Wang, D.A. Cullen, Y.T. Pan, S. Hwang, M.Y. Wang, Z.X. Feng, J.Y. Wang, M. H. Engelhard, H.G. Zhang, Y.H. He, Y.Y. Shao, D. Su, K.L. More, J.S. Spendelow, G. Wu, Nitrogen-coordinated single cobalt atom catalysts for oxygen reduction in proton exchange membrane fuel cells, *Adv. Mater.* 30 (2018) 1706758.
- [6] C. Du, Y. Gao, J. Wang, W. Chen, A new strategy for engineering a hierarchical porous carbon-anchored Fe single-atom electrocatalyst and the insights into its bifunctional catalysis for flexible rechargeable Zn-air batteries, *J. Mater. Chem. A* 8 (19) (2020) 9981–9990.
- [7] X. Ao, W. Zhang, Z. Li, J.-G. Li, L. Soule, X. Huang, W.-H. Chiang, H.M. Chen, C. Wang, M. Liu, X.C. Zeng, Markedly enhanced oxygen reduction activity of single-atom Fe catalysts via integration with Fe nanoclusters, *ACS Nano* 13 (10) (2019) 11853–11862.
- [8] H.Q. Yang, Z.Y. Li, S.Q. Kou, G.L. Lu, Z.N. Liu, A complex-sequestered strategy to fabricate Fe single-atom catalyst for efficient oxygen reduction in a broad pH-range, *Appl. Catal. B* 278 (2020) 119270.
- [9] P. Yin, T. Yao, Y. Wu, L. Zheng, Y. Lin, W. Liu, H. Ju, J. Zhu, X. Hong, Z. Deng, G. Zhou, S. Wei, Y. Li, Single cobalt atoms with precise N-coordination as superior oxygen reduction reaction catalysts, *Angew. Chem. Int. Ed.* 55 (36) (2016) 10800–10805.
- [10] L.i. Jiao, J. Li, L.L. Richard, Q. Sun, T. Stracensky, E. Liu, M.T. Sougrati, Z. Zhao, F. Yang, S. Zhong, H. Xu, S. Mukerjee, Y.u. Huang, D.A. Cullen, J.H. Park, M. Ferrandon, D.J. Myers, F. Jaouen, Q. Ji, Chemical vapour deposition of Fe-N-C oxygen reduction catalysts with full utilization of dense Fe- N_4 sites, *Nat. Mater.* 20 (10) (2021) 1385–1391.
- [11] P. Song, M. Luo, X.Z. Liu, W. Xing, W.L. Xu, Z. Jiang, L. Gu, Zn single atom catalyst for highly efficient oxygen reduction reaction, *Adv. Funct. Mater.* 27 (2017) 1700802.
- [12] P.Q. Liao, J.Q. Shen, J.P. Zhang, Metal-organic frameworks for electrocatalysis, *Coordin. Chem. Rev.* 373 (2018) 22–48.
- [13] S. Dissegna, K. Epp, W.R. Heinz, G. Kieslich, R.A. Fischer, Defective metal-organic frameworks, *Adv. Mater.* 30 (2018) 1704501.
- [14] R. Zhao, Z. Liang, S. Gao, C.e. Yang, B. Zhu, J. Zhao, C. Qu, R. Zou, Q. Xu, Puffing up energetic metal-organic frameworks to large carbon networks with hierarchical porosity and atomically dispersed metal sites, *Angew. Chem.* 131 (7) (2019) 1997–2001.
- [15] Y. Yuan, Q. Zhang, Y. Li, L. Lv, Y. Hou, G.e. Li, J. Fu, L. Yang, Z. Bai, Beads-on-string hierarchical structured electrocatalysts for efficient oxygen reduction reaction, *Carbon Energy* n/a 5 (2) (2023).
- [16] P. Rao, D.X. Wu, T.J. Wang, J. Li, P.L. Deng, Q. Chen, Y.J. Shen, Y. Chen, X.L. Tian, Single atom cobalt electrocatalyst for efficient oxygen reduction reaction, *eScience* 2 (2022) 399–404.
- [17] Q.H. Sun, K. Zhu, X.L. Ji, D.D. Chen, C. Han, T.T. Li, Y. Hu, S.M. Huang, J.J. Qian, MOF-derived three-dimensional ordered porous carbon nanomaterial for efficient alkaline Zinc-air batteries, *Sci. China Mater.* 65 (2022) 1453–1462.
- [18] L. Li, Z. Xu, X.X. Chen, C.H. Fang, D.Y. Yan, G.Y. Xiao, A strategy of bifunctional nanoscale melamine-resin sphere template to fabricate porous carbons, *Adv. Mater. Interfaces* 8 (2021) 2100244.
- [19] H. Jin, H. Zhou, P. Ji, C. Zhang, J. Luo, W. Zeng, C. Hu, D. He, S. Mu, ZIF-8/LiFePO₄ derived Fe-N-P Co-doped carbon nanotube encapsulated Fe₂P nanoparticles for efficient oxygen reduction and Zn-air batteries, *Nano Res.* 13 (3) (2020) 818–823.
- [20] C.Z. Zhu, Q.R. Shi, B.Z. Xu, S.F. Fu, G. Wan, C. Yang, S.Y. Yao, J.H. Song, H. Zhou, D. Du, S.P. Beckman, D. Su, Y.H. Lin, Hierarchically porous M-N-C (M = Co and Fe) single-atom electrocatalysts with robust MN₄ active moieties enable enhanced ORR performance, *Adv. Energy Mater.* 8 (2018) 1801956.
- [21] L.B. Zong, K.C. Fan, W.C. Wu, L.X. Cui, L.L. Zhang, B. Johannessen, D.C. Qi, H. J. Yin, Y. Wang, P.R. Liu, L. Wang, H.J. Zhao, Anchoring single copper atoms to microporous carbon spheres as high-performance electrocatalyst for oxygen reduction reaction, *Adv. Funct. Mater.* 31 (2021) 2104864.
- [22] J. Zhang, Y. Zhao, C. Chen, Y.-C. Huang, C.-L. Dong, C.-J. Chen, R.-S. Liu, C. Wang, K. Yan, Y. Li, G. Wang, Tuning the coordination environment in single-atom catalysts to achieve highly efficient oxygen reduction reactions, *J. Am. Chem. Soc.* 141 (51) (2019) 20118–20126.

- [23] Z. Chen, S. Jiang, G. Kang, D. Nguyen, G.C. Schatz, R.P. Van Duyne, Operando characterization of iron phthalocyanine deactivation during oxygen reduction reaction using electrochemical tip-enhanced raman spectroscopy, *J. Am. Chem. Soc.* 141 (39) (2019) 15684–15692.
- [24] J.-Y. Gu, Z.-F. Cai, D. Wang, L.-J. Wan, Single-molecule imaging of iron-phthalocyanine-catalyzed oxygen reduction reaction by in situ scanning tunneling microscopy, *ACS Nano* 10 (9) (2016) 8746–8750.
- [25] K.J. Chen, K. Liu, P.D. An, H.J. Li, Y.Y. Lin, J.H. Hu, C.K. Jia, J.W. Fu, H.M. Li, H. Liu, Z. Lin, W.Z. Li, J.H. Li, Y.R. Lu, T.S. Chan, N. Zhang, M. Liu, Iron phthalocyanine with coordination induced electronic localization to boost oxygen reduction reaction, *Nat. Commun.* 11 (2020) 4173.
- [26] A. Kumar, G. Yasin, M. Tabish, D. Kumar Das, S. Ajmal, A. Kumar Nadda, G. Zhang, T. Maiyalagan, A. Saad, R.K. Gupta, M.M. Makhlouf, S. Ibraheem, A catalyst-free preparation of conjugated poly iron-phthalocyanine and its superior oxygen reduction reaction activity, *Chem. Eng. J.* 445 (2022) 136784.
- [27] A. Byeon, W.C. Yun, J.M. Kim, J.W. Lee, Recent progress in heteroatom-doped carbon electrocatalysts for the two-electron oxygen reduction reaction, *Chem. Eng. J.* 456 (2023) 141042.
- [28] S. Zhang, M. Chen, X. Zhao, J. Cai, W. Yan, J.C. Yen, S. Chen, Y. Yu, J. Zhang, Advanced noncarbon materials as catalyst supports and non-noble electrocatalysts for fuel cells and metal-air batteries, *Electrochem. Energy Rev.* 4 (2) (2021) 336–381.
- [29] L. Tang, Q. Xu, Y.u. Zhang, W. Chen, M. Wu, MOF/PCP-based electrocatalysts for the oxygen reduction reaction, *Electrochem. Energy Rev.* 5 (1) (2022) 32–81.
- [30] X.Z. Yu, S.J. Lai, S.S. Xin, S. Chen, X.L. Zhang, X.L. She, T.R. Zhan, X.L. Zhao, D. J. Yang, Coupling of iron phthalocyanine at carbon defect site via π - π stacking for enhanced oxygen reduction reaction, *Appl. Catal. B* 280 (2021) 119437.
- [31] J. Guo, X.M. Yan, Q. Liu, Q. Li, X. Xu, L.T. Kang, Z.M. Cao, G.L. Chai, J. Chen, Y. B. Wang, J.N. Yao, The synthesis and synergistic catalysis of iron phthalocyanine and its graphene-based axial complex for enhanced oxygen reduction, *Nano Energy* 46 (2018) 347–355.
- [32] X.Y. Qiu, X.H. Yan, H. Pang, J.C. Wang, D.M. Sun, S.H. Wei, L. Xu, Y.W. Tang, Isolated Fe single atomic sites anchored on highly steady hollow graphene nanospheres as an efficient electrocatalyst for the oxygen reduction reaction, *Adv. Sci.* 6 (2019) 1801103.
- [33] Q. Huang, Y.Y. Guo, D.D. Chen, L.J. Zhang, T.T. Li, Y. Hu, J.J. Qian, S.M. Huang, Rational construction of ultrafine noble metals onto carbon nanoribbons with efficient oxygen reduction in practical alkaline fuel cell, *Chem. Eng. J.* 424 (2021) 130336.
- [34] Y.F. Lin, H. Wan, D. Wu, G. Chen, N. Zhang, X.H. Liu, J.H. Li, Y.J. Cao, G.Z. Qiu, R. Z. Ma, Metal-organic framework hexagonal nanoplates: Bottom-up synthesis, topotactic transformation, and efficient oxygen evolution reaction, *J. Am. Chem. Soc.* 142 (2020) 7317–7321.
- [35] Z. Ristanović, J.P. Hofmann, M.-I. Richard, T. Jiang, G.A. Chahine, T.U. Schüllli, F. Meirer, B.M. Weckhuysen, X-ray excited optical fluorescence and diffraction imaging of reactivity and crystallinity in a zeolite crystal: crystallography and molecular spectroscopy in one, *Angew. Chem. Int. Ed.* 55 (26) (2016) 7496–7500.
- [36] J.Q. Shan, J.W. Liao, C. Ye, J.C. Dong, Y. Zheng, S.Z. Qiao, The dynamic formation from metal-organic frameworks of high-density platinum single-atom catalysts with metal-metal interactions, *Angew. Chem. Int. Ed.* 61 (2022) e202213412.
- [37] J. Gu, C.-S. Hsu, L. Bai, H.M. Chen, X. Hu, Atomically dispersed Fe^{3+} sites catalyze efficient CO_2 electroreduction to CO, *Science* 364 (6445) (2019) 1091–1094.
- [38] X.Y. Xie, L. Shang, X.Y. Xiong, R. Shi, T.R. Zhang, Fe single-atom catalysts on MOF-5 derived carbon for efficient oxygen reduction reaction in proton exchange membrane fuel cells, *Adv. Energy Mater.* 12 (2022) 2102688.
- [39] P.K. Cao, X. Quan, X.W. Nie, K. Zhao, Y.M. Liu, S. Chen, H.T. Yu, J.G. Chen, Metal single-site catalyst design for electrocatalytic production of hydrogen peroxide at industrial-relevant currents, *Nat. Commun.* 14 (2023) 172.
- [40] S.-H. Yin, J. Yang, Y.u. Han, G. Li, L.-Y. Wan, Y.-H. Chen, C. Chen, X.-M. Qu, Y.-X. Jiang, S.-G. Sun, Construction of highly active metal-containing nanoparticles and FeCo-N_4 composite sites for the acidic oxygen reduction reaction, *Angew. Chem. Int. Ed.* 59 (49) (2020) 21976–21979.
- [41] A. Jain, Z. Wang, J.K. Nørskov, Stable two-dimensional materials for oxygen reduction and oxygen evolution reactions, *ACS Energy Lett.* 4 (6) (2019) 1410–1411.
- [42] A. Ignaczak, R. Nazmutdinov, A. Goduljan, L. Moreira de Campos Pinto, F. Juarez, P. Quaino, E. Santos, W. Schmickler, A scenario for oxygen reduction in alkaline media, *Nano Energy* 26 (2016) 558–564.